Boosting the capacity and stability of a MoO₃ cathode *via* valence regulation and polypyrrole coating for a rechargeable Zn ion battery†

Yachen He,[a] Weiwei Xue,[a] Yifeng Huang,[a] Hongwei Tang,[a] Guangxia Wang, [iD][a] Dezhou Zheng,*[a] Wei Xu,[a] Fuxin Wang [iD] *[a] and Xihong Lu [iD][ab]

Molybdenum trioxide (MoO_3) is emerging as a hugely competitive cathode material for aqueous zinc ion batteries (ZIBs) for its high theoretical capacity and electrochemical activity. Nevertheless, owing to its undesirable electronic transport capability and poor structural stability, the practical capacity and cycling performance of MoO_3 are yet unsatisfactory, which greatly blocks its commercial use. In this work, we report an effective approach to first synthesise nanosized MoO_{3-x} materials to provide more active specific surface areas, while improving the capacity and cycle life of MoO_3 by introducing low valence Mo and coated polypyrrole (PPy). MoO_3 nanoparticles with low-valence-state Mo and PPy coating (denoted as MoO_{3-x}@PPy) are synthesized *via* a solvothermal method and subsequent electrodeposition process. The as-prepared MoO_{3-x}@PPy cathode delivers a high reversible capacity of 212.4 mA h g^{-1} at 1 A g^{-1} with good cycling life (more than 75% capacity retention after 500 cycles). In contrast, the original commercial MoO_3 sample only obtains a capacity of 99.3 mA h g^{-1} at 1 A g^{-1}, and a cycling stability of 10% capacity retention over 500 cycles. Additionally, the fabricated Zn//MoO_{3-x}@PPy battery obtains a maximum energy density of 233.6 W h kg^{-1} and a power density of 11.2 kW kg^{-1}. Our results provide an efficient and practical approach to enhance commercial MoO_3 materials as high-performance cathodes for AZIBs.

Introduction

With the rapid development of wind, water, and solar energy, along with other forms of clean energy, the need for corresponding electrochemical energy storage technology has become extremely urgent.[1,2] Additionally, increased demands for the development of this technology have been raised due to the electrification of transportation tools and the growing intelligence of electronic devices.[3] Rechargeable lithium-ion batteries are already extensively utilized in energy storage devices on account of the advantages of their high energy density.[4] Nevertheless, the limited resources of lithium elements, as well as safety concerns associated with the use of high-cost organic electrolytes, have restricted the further development of lithium-ion batteries.[5] Compared with organic batteries, aqueous batteries use an aqueous solution as the electrolyte,[6] which have remarkable merits of high safety,

inexpensive, eco-friendly, and simple packaging.[7] The superior ionic conductivity of aqueous solutions gives them excellent rate performance.[8] In recent years, aqueous secondary batteries, including monovalent ion (Li^+, Na^+, K^+) and multivalent ion (Ca^{2+}, Zn^{2+}, Mg^{2+}, Al^{3+}) batteries, have attracted a lot of attention.[9,10] Among them, aqueous zinc ion batteries (AZIBs) are growing rapidly for the advantages of inexpensive,[11] low potential (-0.76 V *vs.* SHE),[12,13] high capacity (820 mA h g^{-1}),[14] and good stability in aqueous solutions of zinc anode,[15] making them suitable for the broad scope of use in large-scale grid energy storage as well as flexible and wearable electronic devices.[16]

As an innovative energy storage device, AZIBs currently have limited range of materials suitable as cathode materials for zinc ion storage.[17] They are mainly consist of manganese-based oxides,[18] vanadium-based oxides,[19] molybdenum-based oxides,[1] Prussian blue and its analogues,[20] and organic oxides.[21] Among them, molybdenum trioxide (MoO_3) has the advantages of high abundance,[22] low toxicity and easy recovery,[23] as well as its multivalent states and two-dimensional layered structure.[24] Nevertheless, MoO_3 suffers from a serious drawback that it tends to dissolve in neutral or weakly acidic electrolytes to destroy its structure,[25] resulting in low actual capacity and poor cycling stability.[26] In previous studies, the electrochemical performance of electrode materials have been

[a]School of Applied Physics and Materials, Wuyi University, Jiangmen 529020, PR China. E-mail: wangfux91@126.com

[b]MOE of the Key Laboratory of Bioinorganic and Synthetic Chemistry, The Key Lab of Low-carbon Chem & Energy Conservation of Guangdong Province, School of Chemistry, Sun Yat-Sen University, Guangzhou 510275, PR China

generally boosted by means of modifications such as morphology modulation,[27] interfacial engineering,[28] valence modulation,[29] doping and coating,[30] and composites.[31] As an instance, Liu *et al.* reported that MoO_3 can exhibit an initial discharge capacity of 120 mA h g^{-1}, but its capacity decreases sharply over 5 cycles of charging/discharging, mainly due to the structure damage.[26] Liu *et al.* used a surface engineering to avoid the structure damage of electrode material through coating a layer of Al_2O_3 on the surface of MoO_3. Through the DFT calculations, MoO_{3-x} obtain a lower Gibbs free energy of Zn^{2+} adsorption on the surface of MoO_{3-x}, indicating that the desorption of Zn^{2+} on MoO_{3-x} is thermodynamically more beneficial and its adsorption/desorption of Zn^{2+} is more reversibility. In addition, it leads to a narrower of the band gap between the valence band and the conduction band, which facilitates the excitation of charge carriers to the conduction band and thus improves the electrical conductivity of MoO_{3-x}.[32] The assembled $Zn//P\text{-}MoO_{3-x}@Al_2O_3$ battery shows improved cycling stability. The capacity retention of $Zn//P\text{-}MoO_{3-x}@Al_2O_3$ battery was 69.2% over 100 cycles, which is better than that of that of $Zn//P\text{-}MoO_{3-x}$ battery (only 40.8%).[32] He *et al.* developed an effective strategy for quasi-solid $PVA/ZnCl_2$ gel electrolyte to stabilize MoO_3 nanowires instead of aqueous electrolyte, and the capacity retention of the assembled $MoO_3//Zn$ battery reach to 70.4% in gel electrolyte over 400 cycles, but only 27.1% in aqueous electrolyte.[33] In addition, Zhang *et al.* developed WP-MoO_3 electrodes by a water-proton co-pre-insertion strategy. WP-MoO_3 electrode achieve selective hydrated proton insertion by using water molecules between the layers to increase the insertion energy barrier of zinc ions by blocking the transport path of zinc ions. Based on the above merits, the capacity retention of the prepared battery is 83% after 1000 cycles.[34] Despite the impressive progress of these works, there is still room to enhance the capacity and cycle stability of MoO_3. Moreover, exploring simpler and practical ways to boost the electrochemical performance of MoO_3 electrodes remains a meaningful challenge.[35]

In this work, we focus on improving the capacity and cycling stability of commercial MoO_3 through a simple and effective approach. Low-valent state enriched and polymer coated MoO_3 electrode materials ($MoO_{3-x}@PPy$) are synthesized by a simple solvothermal method and subsequent electrodeposition process. The reactivity and structural stability of $MoO_{3-x}@PPy$ electrodes are boosted with the help of low-valence-state Mo introduction and coating strategies. Firstly, the solvothermal reaction allows the MoO_3 particles to be nanosized to obtain more active sites, while the introduction of low-valent molybdenum improves the reactivity of the electrode material. Secondly, the coated PPy layer improves the stability of the electrode material in the electrolyte. Combing the above advantages, the assembled $Zn//MoO_{3-x}@PPy$ battery obtain a high reversible capacity of 212.4 mA h g^{-1} at 1 A g^{-1} and favorable cycle life of 75% capacity retention over 500 cycles, while that of $Zn//MoO_3$ battery is only 99.3 mA h g^{-1} at 1 A g^{-1} and 10% capacity retention over 500 cycles. Moreover, the fabricated $Zn//MoO_{3-x}@PPy$ battery exhibits a maximum

energy density of 233.6 W h kg^{-1} and power density of 11.2 kW kg^{-1}.

Experimental section

Preparation of MoO_{3-x} electrode

All chemicals in this work were utilized without any purification (the chemicals were 99% pure). 0.3 g of commercial MoO_3 powder was added to a mixed solution of 10 ml of water and 10 ml of ethylene glycol. After stirring magnetically for 30 min at room temperature, the homogeneous mixed solution was poured into an autoclave lined with polytetrafluoroethylene and then placed in a blast drying oven at 180 °C for 12 h. After it cooled down, the powder was washed repeatedly with deionized water and anhydrous ethanol after centrifugation, and then set it in an oven at 60 °C for 6 h to obtain black MoO_{3-x} powder. After that, the obtained MoO_{3-x} powder, acetylene black and polyvinylidene fluoride (PVDF) were mixed and ground in the ratio of 8 : 1 : 1 by mass. Then, the above mixture powder was added to *N*-methylpyrrolidone (NMP) solution to form a uniform slurry. Then the obtained slurry was homogeneously coated on carbon paper and dried in a vacuum oven for 6 h to obtain MoO_{3-x} electrode.

Preparation of $MoO_{3-x}@PPy$ electrode

The above prepared MoO_{3-x} electrode (1 × 2 cm) was electro-deposited in a homogeneous electrolyte formed by mixing and stirring 0.1 M sodium sulfate and 0.145 M pyrrole. The deposition process was performed using cyclic voltammetry with a voltage window of −0.5 to 0.8 V for 4 segments at 50 mV s^{-1}, resulting in the electrodeposition of PPy coating on the surface of the MoO_{3-x} electrode material ($MoO_{3-x}@PPy$).

Characterization of the material

The surface morphology, microstructure, and elemental distribution of electrode materials are characterized by Scanning electron microscopy (SEM, Sigma500, ZEISS) equipped with X-ray energy spectrometry (EDS, INCA 300, Oxford Instruments) and transmission electron microscope (TEM, JEM-F200, JEOL) analysis. The crystal structure of the prepared electrode materials is measured by X-ray diffraction analysers (XRD, Bruker Germany) equipped with a Cu-Kα radiation source. X-ray photoelectron spectroscopy (XPS, NEXSA, Thermo VG) and Fourier Transform infrared spectroscopy (FTIR, NICOLET 6700) were utilized to investigate the elemental composition and functional groups of prepared electrode materials.

Electrochemical tests

The cathode material has an active substance loading of about 2 mg cm^{-2}. Electrochemical characterization techniques such as cyclic voltammetry (CV), electrochemical impedance spectroscopy (EIS), and galvanostatic charge/discharge (GCD) tests were conducted on an electrochemical workstation (CHI660E) with a potential window of 0.2–1.3 V using AZIBs packed in air with pure MoO_3, fabricated MoO_{3-x}, and fabricated

MoO_{3-x}@PPy as cathodes, zinc plates as anodes, and 2 M $ZnSO_4$ as the electrolyte.

Results and discussion

The synthesis of MoO_{3-x}@PPy electrode consists of a two-step synthesis process as shown in Fig. 1a. Firstly, the MoO_{3-x} electrode material enriched in the low-valence-state Mo was synthesized by solvothermal reaction of commercial MoO_3 with ethylene glycol. The free molybdenum produced by the dissolving of commercial MoO_3 is partially reduced by ethylene glycol in solution, which resulted in the synthesis of MoO_{3-x} electrode material. Subsequently, it was coated with acetylene black and PVDF in the ratio of 8 : 1 : 1 on carbon paper to produce MoO_{3-x} electrode. A comparison of SEM image of commercial MoO_3 electrode (Fig. S1†) and MoO_{3-x} electrode (Fig. 1b and d) shows that the particles of MoO_{3-x} electrode materials become smaller after the solvent heat treatment. Secondly, the conducting polymer PPy was deposited on the surface of the MoO_{3-x} electrode with an electrodeposition process. As shown in Fig. 1c and e, the morphology of the electrode material is almost unchanged after PPy deposition, implying that the polymer coating has not changes the microscopic morphology of the MoO_{3-x} electrode material.

To further investigate the microstructure and crystal type of the material, the synthesized material was characterized by TEM and XRD. Fig. S2† shows a TEM image of commercial MoO_3 showing a particle size of approximately 150 nm. In addition, a lattice stripe of 0.133 nm is visible in the HRTEM image of MoO_3, which corresponds to the (202) crystal plane of MoO_3 (JCPDF # 05-0508), while the calibrated diffraction points in selected electron diffraction (SAED) pattern of the MoO_3 material correspond to the to the (150), (210) and (110) crystal
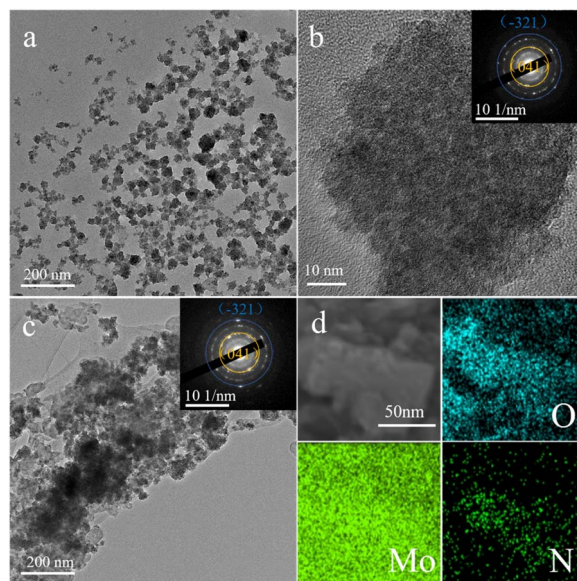

Fig. 2 (a) TEM and (b) HRTEM images of MoO_{3-x} material (inset the SAED pattern). (c) TEM image of MoO_{3-x}@PPy material (inset the SAED pattern). (d) The corresponding area EDS mapping.

planes of MoO_3 (JCPDF # 05-0508). Fig. 2a and b shows a TEM image of MoO_{3-x}, showing a particle size of approximately 50 nm, which is much smaller than the commercial MoO_3 material and in line with the SEM results. However, SAED pattern of the MoO_{3-x} material shows two distinct diffraction rings corresponding to the (−321) crystal plane of MoO_2 (JCPDS # 32-0671) and the (041) crystal plane of MoO_3 (JCPDF # 05-0508), indicating the introduction of low-valent-state Mo after solvothermal reaction. Fig. 2c shows a TEM image of MoO_{3-x}@PPy showing a thin film outside the MoO_{3-x} material, demonstrating that PPy is encapsulated on the surface of the MoO_{3-x} electrode material. Subsequently, the elemental distribution in the MoO_{3-x}@PPy material was analyzed by energy density spectroscopy (EDS). The results display that the O, Mo and N elements are evenly dispersed on the electrode material, again proving that PPy is evenly coated on the MoO_{3-x} electrode material. The crystallization pattern of the prepared materials was investigated more thoroughly by XRD test. Fig. 3a shows the XRD patterns of commercial MoO_3, MoO_{3-x}, and MoO_{3-x}@PPy materials. It is noteworthy that the MoO_{3-x} sample synthesized after the solvothermal reaction contains a large number of characteristic peaks (−111), (200), and (211) of MoO_2 (JCPDS # 32-0671) peaks and a small number of characteristic peaks (110), (040), and (112) of MoO_3, while only characteristic peaks of MoO_3 (JCPDF # 05-0508) are present in the commercial MoO_3, which implies the successful introduction of low-valent-state Mo in the commercial MoO_3 by the solvothermal reaction. In addition, the XRD pattern of MoO_{3-x}@PPy material after electrodeposition of PPy shows a decrease in peak intensity, but characteristic peaks of MoO_2 (−111), (200), (211) and MoO_3 (112) still can be found in the sample, which indicates that the coated amorphous PPy do not change the crystal structure, which is in line with the results of
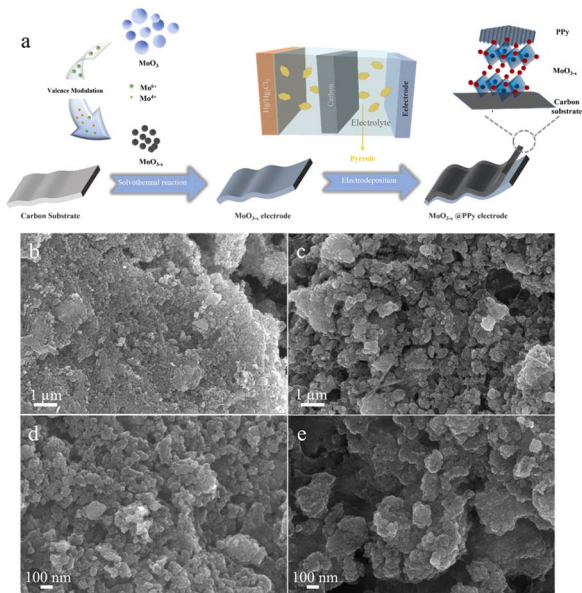

Fig. 1 (a) Schematic illustration of the synthesis of MoO_{3-x}@PPy electrode material. (b and d) SEM images of MoO_{3-x} electrode material. (c and e) SEM images of MoO_{3-x}@PPy electrode material.

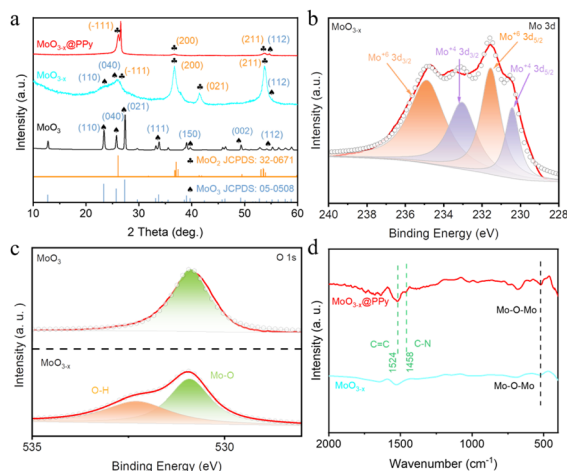**Fig. 3** (a) XRD patterns corresponding to MoO_3, MoO_{3-x} and MoO_{3-x}@PPy samples. (b) Mo 3d spectra of the synthesized MoO_{3-x} sample. (c) O 1s spectra of MoO_3 and MoO_{3-x} samples. (d) FI-IR of MoO_{3-x} and MoO_{3-x}@PPy samples.

TEM test. Furthermore, XPS was utilized to analyses the valence and elemental composition of the material. As shown in Fig. 3b and S3b,† the Mo 3d spectrum of commercial MoO_3 matches the two characteristic peaks of $3d_{5/2}$ and $3d_{3/2}$ of Mo^{6+} at 232.75 and 235.93 eV respectively,[36] indicating that molybdenum is predominantly present in commercial MoO_3 at +6 valence. However, the MoO_{3-x} sample produced by solvothermal reduction with ethylene glycol showed two additional peaks in its Mo 3d spectrum. Of these, 230.43 and 233.13 eV correspond to the $3d_{3/2}$ and $3d_{5/2}$ characteristic peaks of Mo^{4+}.[37] The presence of Mo^{4+} indicates the introduction of low-valence-state Mo into the material. Furthermore, according to the analysis of the XPS test, the two characteristic peaks of Mo^{6+} are still found at 232.64 and 235.41 eV, which implies that the commercial MoO_3 has not been completely reduced to MoO_2. Fig. S3a† displays the XPS survey spectra of MoO_3 and MoO_{3-x}@PPy electrode material, which shows that only the material of MoO_3@PPy contains N elements, indicating the successful coated of PPy.[38] Also Fig. S3c† shows the Mo 3p spectra of MoO_3 and MoO_{3-x}@PPy. The Mo 3p peak is sharper for MoO_3, while the distinct hump at 397.5 eV in the Mo 3p XPS spectrum of MoO_{3-x}@PPy further confirms the presence of N on the MoO_{3-x}@PPy surface.[39] The O 1s spectra of the MoO_3 and MoO_{3-x} samples in Fig. 3c show that for 530.8 ± 0.1 eV (green area fraction) the binding energy component is derived from the lattice oxygen (O_a) of MoO_3, for the MoO_{3-x} sample the peak at 532.2 ± 0.1 eV (yellow area fraction) is associated with a chemically absorbed oxygen site (O_c).[38] Fig. 3d shows the Fourier transform infrared spectra (FT-IR) of MoO_{3-x} and MoO_{3-x}@PPy electrode materials. The FT-IR spectra of both electrode materials show the core characteristic peaks of molybdenum oxide (Mo–O–Mo), while the main characteristic peaks of PPy (C=C and C–N) are also observed in the MoO_{3-x}@PPy electrode,[40] again demonstrating that PPy was successfully coated on the surface of the MoO_{3-x} material.

To further investigate the effects of low-valence-state Mo introduction and PPy coating strategies on the zinc storage property of commercial MoO_3 materials, a series of AZIBs based on the synthesized MoO_3, MoO_{3-x}, and MoO_{3-x}@PPy materials MoO_3 as cathode, zinc plate as anode and 2 M $ZnSO_4$ as electrolyte were assembled. First, we optimised the thickness of the electrodeposition PPy layers. As shown in Fig. S4,† its electrochemical property decreases as the number of deposition cycles increases, indicating that too thick PPy will hinder MoO_{3-x} from participating in the electrochemical reaction. However, PPy layer with appropriate thickness (2 cycles of electrodeposition) can not only stabilize the structural stability of MoO_{3-x} in electrolyte, but also provide additional zinc storage performance. Fig. 4a shows the CV curves of assembled Zn//MoO_3, Zn//MoO_{3-x}, and Zn//MoO_{3-x}@PPy batteries at 20 mV s^{-1} within the operating window of 0.2–1.3 V.

The graph clearly shows that the CV curves of the three batteries are almost identical in shape, but the current response signal gradually enlarges as the introduction of the low-valence-state Mo and the PPy coating, indicating that their zinc storage performance gradually enhanced. Then, the GCD curves in Fig. 4b shows more clearly that the Zn//MoO_{3-x}@PPy battery achieves a highest discharge capacity of 212.4 mA h g^{-1} (based on the mass of the cathode active material) at 1 A g^{-1}, while that of Zn//MoO_{3-x} and Zn//MoO_3 batteries are only 181.7 mA h g^{-1} and 99.3 mA h g^{-1}, respectively. These results demonstrate that
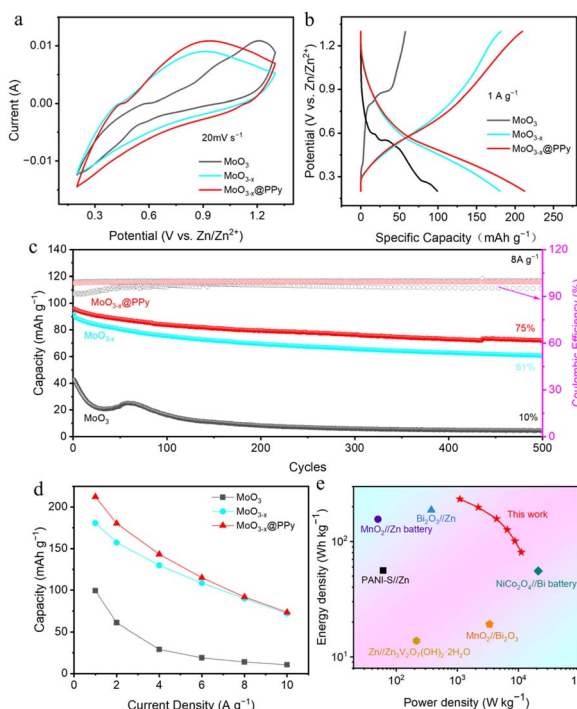

Fig. 4 (a) CV curves of Zn//MoO_3, Zn//MoO_{3-x} and Zn//MoO_{3-x}@PPy batteries at 20 mV s^{-1}. (b) GCD curves of Zn//MoO_3, Zn//MoO_{3-x} and Zn//MoO_{3-x}@PPy batteries at 1A g^{-1}. (c) Cycle performance of Zn//MoO_3, Zn//MoO_{3-x} and Zn//MoO_{3-x}@PPy batteries at 8 A g^{-1}. (d) Rate performance of Zn//MoO_3, Zn//MoO_{3-x} and Zn//MoO_{3-x}@PPy batteries. (e) Ragone plots of the fabricated Zn//MoO_{3-x}@PPy battery in this work compared to other reported batteries.

the introduce of low-valence-state Mo and PPy coating strategies can boost the Zn storage capacity of commercial MoO_3. Furthermore, the rate performance of the fabricated three kinds of batteries was characterized at different current densities, illustrated in Fig. 4d, where the $Zn//MoO_{3-x}$@PPy shown highest capacities at all currents. The reversible specific capacities of $Zn//MoO_{3-x}$@PPy battery can reach 212.4 mA h g^{-1} to 73.3 mA h g^{-1} at the current density of 1 to 10 A g^{-1}, respectively. In particular, $Zn//MoO_{3-x}$@PPy battery exhibited 35% capacitance retention even at a high current density of 10 A g^{-1}. By contrast, $Zn//MoO_3$ battery achieved specific capacities of 99.3 mA h g^{-1} to 10.5 mA h g^{-1} at 1 to 10 A g^{-1}, respectively. Its rate property is only 10.6%, again indicating that the low-valence-state Mo introduction and PPy coating strategies can boost the capacity and rate property of commercial MoO_3 for zinc storage. Much encouragingly, the $Zn//MoO_{3-x}$@PPy battery maintained 75% capacity retention over 500 cycles, while that of $Zn//MoO_3$ and $Zn//MoO_{3-x}$ batteries were not high, 61% and 10%, respectively, indicating that coating with a corrosion resistant polymer coating is a very simple and practical way to enhance the stability of electrode materials (Fig. 4c). It is worth noting that the specific capacity of MoO_3 is improved over the first 100 cycles, which might attribute to the continuous activation of the electrode due to the surface chemical reactions between MoO_3 and the $ZnSO_4$ electrolyte.[41] Energy density and power density are the two vital parameters for evaluating the energy storage capacity of batteries. As shown in Fig. 4e, the fabricated $Zn//MoO_{3-x}$@PPy battery obtained an energy density of up to 233.6 W h kg^{-1} (power density of 1.1 kW kg^{-1}) and the maximum power density of 11.2 kW kg^{-1} (energy density of 80.6 W h kg^{-1}), exceed those of some newly published aqueous batteries, as shown in Table 1. This satisfactory energy density and power density are expected to enable our designed $Zn//MoO_{3-x}$@PPy battery to become a more practical alternative power source.

The electrochemical kinetics of the fabricated electrode were further investigated by conducting CV measurements at various scan rates ranging from 1 to 10 mV s^{-1} (displayed in Fig. 5a and S5†). As can clearly be seen the figure of the CV curve at any scan rates is essentially the same, but the peaks are slightly shifted. The diffusion and pseudocapacitance behaviour of the battery during the charge/discharge cycle was distinguished by adjusting the scan rate to correspond to the response of the
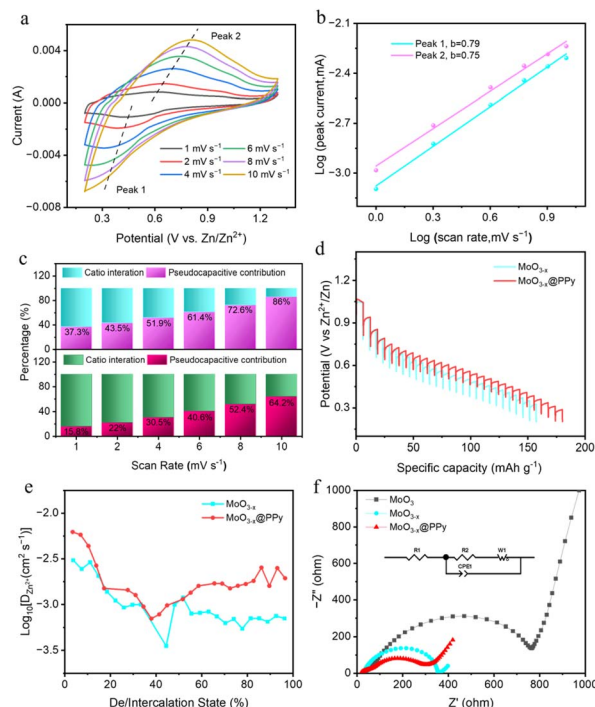
Table 1 The energy density and power density of the $Zn//MoO_{3-x}$@PPy battery and other reported batteries

ZIBs	Power density (W kg^{-1})	Energy density (W kg^{-1})	Ref.
MnO_2//Zn battery	50	156.1	42
Bi_2O_3//Zn battery	375	187.5	43
PANI-S//Zn battery	61	56	44
Ni//Fe battery	3370	19.1	45
$NiCo_2O_4$//Bi battery	21 200	55.4	46
$Zn//Zn_3V_2O_7(OH)_2$–$2H_2O$ battery	214	13.8	47
This work	11 000	233.6	

Fig. 5 (a) CV curves for MoO_{3-x}@PPy at a range of scan rates of 1, 2, 4, 6, 8 and 10 mV s^{-1}. (b) $\log(i)$ vs. $\log(v)$ plots of the two peaks in the CV curve for MoO_{3-x}@PPy. (c) Ratio of diffusion contribution to capacitance contribution for $Zn//MoO_{3-x}$ and $Zn//MoO_{3-x}$@PPy. (d) Discharge GITT curves for $Zn//MoO_{3-x}$ and $Zn//MoO_{3-x}$@PPy at a current density of 2 A g^{-1} and (e) corresponding Zn^{2+} coefficients $D_{Zn^{2+}}$. (f) Nyquist plots of MoO_3, MoO_{3-x} and MoO_{3-x}@PPy.

peak current. In the case of a dominant battery behaviour, the relationship between peak current i and scan voltage v follows a power function of 0.5, indicating that diffusion plays an important role throughout the process. When analyzing battery behavior during charge/discharge cycles, it is possible to distinguish between diffusive and pseudo-capacitive behavior by adjusting the scan rate to match peak current response. In cases where the process is dominated by capacitance, peak current i varies linearly with scanning voltage v. To determine the presence of pseudo-capacitive behavior, researchers can calculate the b value using the equation $i = av^b$. This allows for a more accurate understanding of electrode material behavior during charging and discharging. When the value of b equals 0.5, the electrode material displays battery characteristics. If the value of b falls among 0.5 to 1, both battery and pseudocapacitive properties can be observed in the electrode material. When b is greater than or equal to 1, the electrode material mainly displays pseudocapacitive behavior. Fig. 5b displays the fitted CV curves for the MoO_{3-x}@PPy samples at different scan rates. It is noteworthy that the calculated b value of the reduction peak is 0.79, suggesting that a blend of both diffusion-controlled and capacity-based kinetic phenomena occurred. To determine the pseudo-capacitance contribution of MoO_{3-x}@PPy at various scan rates, the pseudo-capacitance equation was utilized: $i = k_1v + k_2v^{1/2}$. This equation takes into account k_1 and k_2 as constants, with k_1v representing the

theoretical value of the pseudo-capacitance contribution. Fig. 5c and S5† showcase the outcomes of this calculation for Zn//MoO$_3$, Zn//MoO$_{3-x}$, and Zn//MoO$_{3-x}$@PPy batteries with varying scan rates ranging from 1 to 10 mV s^{-1}. Upon comparison of the pseudocapacitance contribution at a scan rate of 10 mV s^{-1}, it is evident that the Zn//MoO$_{3-x}$@PPy battery exhibits the highest pseudocapacitance contribution, indicating superior rate performance. This finding corroborates with the data presented in Fig. 4d. Additionally, it is worth noting that the Zn//MoO$_{3-x}$@PPy battery achieves a significant capacitance contribution of 86% at 10 mV s^{-1}, further highlighting the dominance of pseudocapacitance in determining its performance (Fig. S6†). Notably, this observation is consistent with the outcomes obtained from our experiments and analysis. The MoO$_{3-x}$@PPy active material possesses a pseudo-capacitive nature that facilitates selective storage of Zn^{2+} ions at the electrode surface. This results in a shortened ion transport distance and an enhanced electron transport rate, ultimately leading to improved rate capabilities and longer cycle life of the electrode material. Zn^{2+} diffusion coefficients $D_{Zn^{2+}}$ in the MoO$_3$, MoO$_{3-x}$ and MoO$_{3-x}$@PPy cathodes were also investigated through the galvanostatic intermittent titration technique (GITT). From Fig. 5d and S7,† all three electrodes exhibit a curve shape similar to the GCD curve (Fig. 4b). The ion diffusion coefficient of the MoO$_{3-x}$@PPy electrode consistently surpasses that of the MoO$_3$ and MoO$_{3-x}$ electrode, indicating that the ion diffusion rate is enhanced by coating it with PPy and low-valence-state Mo introduction (Fig. 5e and S7†). The electrochemical impedance spectroscopy (EIS) data for all electrode materials is presented in Fig. 5f. This figure clearly illustrates that the MoO$_{3-x}$@PPy electrode exhibits a smaller semicircle in the high frequency region, which indicates a lower charge transfer resistance (R_{ct}). The R_{ct} of MoO$_{3-x}$@PPy is approximately 278.3 Ω, lower than that of MoO$_{3-x}$ (357.5 Ω) and commercial MoO$_3$ (769.9 Ω), demonstrating that the R_{ct} of the MoO$_{3-x}$@PPy electrode material can be greatly boosted by the low-valence-state Mo introduction and PPy coating strategies. Furthermore, in the low frequency region, the MoO$_{3-x}$@PPy electrode demonstrates a steep linear slope, implying efficient electron diffusion capability. This is in contrast to the other electrode materials tested, which exhibit a lower and less steep slope in this region.

Conclusions

In this work, we synthesized high capacity, long cycle life PPy coated low-valent-state Mo enriched composites MoO$_{3-x}$@PPy as cathode materials for AZIBs by a simple and effective solvothermal and electrodeposition method in two steps. With the help of low-valence-state Mo introduction and PPy coating to synergistically enhanced the capacity and cycling life of commercial MoO$_3$. The Zn//MoO$_{3-x}$@PPy battery assembled based on MoO$_{3-x}$@PPy as the cathode material exhibited a high capacity of 212.4 mA h g^{-1} at 1 A g^{-1} and outstanding rate performance (73.3 mA h g^{-1} capacity even at 10 A g^{-1}). Encouragingly, the Zn//MoO$_{3-x}$@PPy battery exhibits excellent cycling life with a capacity retention rate of 75% after 500 cycles.

Meanwhile, the Zn//MoO$_3$ battery assembled based on commercial MoO$_3$ has only 99.3 mA h g^{-1} capacity at 1 A g^{-1} and 10% capacitance retention (after 500 cycles). Moreover, the prepared battery exhibited favorable energy density of 233.6 W h kg^{-1}. This work shows practical strategies to boost the zinc storage property of commercial MoO$_3$, providing new ideas and approaches for its commercialization.

Conflicts of interest

There are no conflicts to declare.

Acknowledgements

Notes and references

1 Z. Fang, C. Liu, X. Li, L. Peng, W. Ding, X. Guo and W. Hou, *Adv. Funct. Mater.*, 2022, **33**, 2210010.
2 X. Wang, Z. Zhang, B. Xi, W. Chen, Y. Jia, J. Feng and S. Xiong, *ACS Nano*, 2021, **15**, 9244–9272.
3 X. Jia, C. Liu, Z. G. Neale, J. Yang and G. Cao, *Chem. Rev.*, 2020, **120**, 7795–7866.
4 X. Li, Z. Huang, C. E. Shuck, G. Liang, Y. Gogotsi and C. Zhi, *Nat. Rev. Chem.*, 2022, **6**, 389–404.
5 M. Zhou, S. Guo, J. Li, X. Luo, Z. Liu, T. Zhang, X. Cao, M. Long, B. Lu and A. Pan, *Adv. Mater.*, 2021, **33**, 2100187.
6 C. Liu, Z. Neale, J. Zheng, X. Jia, J. Huang, M. Yan, M. Tian, M. Wang, J. Yang and G. Cao, *Energy Environ. Sci.*, 2019, **12**, 2273–2285.
7 K. Ouyang, D. Ma, N. Zhao, Y. Wang, M. Yang, H. Mi, L. Sun, C. He and P. Zhang, *Adv. Funct. Mater.*, 2022, **32**, 2109749.
8 J. Cao, D. Zhang, X. Zhang, Z. Zeng, J. Qin and Y. Huang, *Energy Environ. Sci.*, 2022, **15**, 499–528.
9 H. Chen, C. Dai, F. Xiao, Q. Yang, S. Cai, M. Xu, H. J. Fan and S. J. Bao, *Adv. Mater.*, 2022, **34**, 2109092.
10 X. Zhang, T. Xiong, B. He, S. Feng, X. Wang, L. Wei and L. Mai, *Energy Environ. Sci.*, 2022, **15**, 3750–3774.
11 Y. Tian, Y. An, C. Wei, B. Xi, S. Xiong, J. Feng and Y. Qian, *Adv. Energy Mater.*, 2021, **11**, 2002529.
12 S. Zhou, Y. Wang, H. Lu, Y. Zhang, C. Fu, I. Usman, Z. Liu, M. Feng, G. Fang and X. Cao, *Adv. Funct. Mater.*, 2021, **31**, 2104361.
13 M. Chen, J. Chen, W. Zhou, X. Han, Y. Yao and C. P. Wong, *Adv. Mater.*, 2021, **33**, 2007559.

14 J. Huang, Z. Guo, Y. Ma, D. Bin, Y. Wang and Y. Xia, *Small Methods*, 2019, **3**, 1800272.

15 X. Yang, C. Li, Z. Sun, S. Yang, Z. Shi, R. Huang, B. Liu, S. Li, Y. Wu and M. Wang, *Adv. Mater.*, 2021, **33**, 2105951.

16 P. Wang, S. Liang, C. Chen, X. Xie, J. Chen, Z. Liu, Y. Tang, B. Lu and J. Zhou, *Adv. Mater.*, 2022, **34**, 2202733.

17 R. Guo, X. Liu, F. Xia, Y. Jiang, H. Zhang, M. Huang, C. Niu, J. Wu, Y. Zhao and X. Wang, *Adv. Mater.*, 2022, **34**, 2202188.

18 F. Gao, B. Mei, X. Xu, J. Ren, D. Zhao, Z. Zhang, Z. Wang, Y. Wu, X. Liu and Y. Zhang, *Chem. Eng. J.*, 2022, **448**, 137742.

19 W. Liang, D. Rao, T. Chen, R. Tang, J. Li and H. Jin, *Angew. Chem., Int. Ed.*, 2022, **61**, e202207779.

20 M. Wu, G. Zhang, H. Yang, X. Liu, M. Dubois, M. A. Gauthier and S. Sun, *InfoMat*, 2022, **4**, e12265.

21 Y. Zhao, Y. Huang, F. Wu, R. Chen and L. Li, *Adv. Mater.*, 2021, **33**, 2106469.

22 X. Chen, J. Zhu, J. Cai, Y. Zhang and X. Wang, *J. Energy Storage*, 2021, **40**, 102721.

23 M. R. Dunkin, J. Kuang, S. Yan, S. T. King, L. M. Housel, L. Ma, S. N. Ehrlich, J. S. Okasinski, K. J. Takeuchi and E. S. Takeuchi, *Adv. Mater. Interfaces*, 2022, **9**, 2201125.

24 W. Xu, K. Zhao and Y. Wang, *Energy Storage Mater.*, 2018, **15**, 374–379.

25 Y. Liu, G. He, H. Jiang, I. P. Parkin, P. R. Shearing and D. J. Brett, *Adv. Funct. Mater.*, 2021, **31**, 2010445.

26 W. Liu, J. Hao, C. Xu, J. Mou, L. Dong, F. Jiang, Z. Kang, J. Wu, B. Jiang and F. Kang, *Chem. Commun.*, 2017, **53**, 6872–6874.

27 D. Chen, M. Lu, D. Cai, H. Yang and W. Han, *J. Energy Chem.*, 2021, **54**, 712–726.

28 Z. Kang, C. Wu, L. Dong, W. Liu, J. Mou, J. Zhang, Z. Chang, B. Jiang, G. Wang and F. Kang, *ACS Sustainable Chem. Eng.*, 2019, **7**, 3364–3371.

29 P. He, Q. Chen, M. Yan, X. Xu, L. Zhou, L. Mai and C.-W. Nan, *EnergyChem*, 2019, **1**, 100022.

30 C. Li, X. Zhang, W. He, G. Xu and R. Sun, *J. Power Sources*, 2020, **449**, 227596.

31 Y. Li, J. Zhang, Q. Chen, X. Xia and M. Chen, *Adv. Mater.*, 2021, **33**, 2100855.

32 Y. Liu, J. Wang, Y. Zeng, J. Liu, X. Liu and X. Lu, *Small*, 2020, **16**, 1907458.

33 X. He, H. Zhang, X. Zhao, P. Zhang, M. Chen, Z. Zheng, Z. Han, T. Zhu, Y. Tong and X. Lu, *Adv. Sci.*, 2019, **6**, 1900151.

34 H. Zhang, W. Wu, Q. Liu, F. Yang, X. Shi, X. Liu, M. Yu and X. Lu, *Angew. Chem., Int. Ed.*, 2021, **60**, 896–903.

35 L. E. Blanc, D. Kundu and L. F. Nazar, *Joule*, 2020, **4**, 771–799.

36 W. Liu, Z. Zhang, J. Shi, Y. Zheng, Y. Wu, X. Fu, N. Liu, J. Su and Y. Gao, *J. Mater. Chem. A*, 2022, **10**, 4043–4052.

37 C. Xia, Y. Zhou, D. B. Velusamy, A. A. Farah, P. Li, Q. Jiang, I. N. Odeh, Z. Wang, X. Zhang and H. N. Alshareef, *Nano Lett.*, 2018, **18**, 1506–1515.

38 Y. Liu, Y. Wang, Y. Meng, R. Plamthottam, W. W. Tjiu, C. Zhang and T. Liu, *ACS Appl. Mater. Interfaces*, 2022, **14**, 4490–4499.

39 C. Tang, L. Zhong, B. Zhang, H. F. Wang and Q. Zhang, *Adv. Mater.*, 2018, **30**, 1705110.

40 X. Mu, Y. Song, Z. Qin, J. Meng, Z. Wang and X.-X. Liu, *Chem. Eng. J.*, 2023, **453**, 139575.

41 Z. Yao, W. Zhang, X. Ren, Y. Yin, Y. Zhao, Z. Ren, Y. Sun, Q. Lei, J. Wang, L. Wang, T. Ji, P. Huai, W. Wen, X. Li, D. Zhu and R. Tai, *ACS Nano*, 2022, **16**, 12095–12106.

42 L. Xu, N. Xu, C. Yan, W. He, X. Wu, G. Diao and M. Chen, *J. Electroanal. Chem.*, 2021, **888**, 115196.

43 D. Zhou, Q. Lu, Z. Li, M. Zhao, S. Li, K. Yin and C. Teng, *Chem.–Eur. J.*, 2023, **29**, e202203500.

44 H. Y. Shi, Y. J. Ye, K. Liu, Y. Song and X. Sun, *Angew. Chem., Int. Ed.*, 2018, **130**, 16597–16601.

45 X. Wu, H. B. Wu, W. Xiong, Z. Le, F. Sun, F. Liu, J. Chen, Z. Zhu and Y. Lu, *Nano Energy*, 2016, **30**, 217–224.

46 Y. Zeng, Z. Lin, Y. Meng, Y. Wang, M. Yu, X. Lu and Y. Tong, *Adv. Mater.*, 2016, **28**, 9188–9195.

47 B. Sambandam, V. Soundharrajan, S. Kim, M. H. Alfaruqi, J. Jo, S. Kim, V. Mathew, Y.-k. Sun and J. Kim, *J. Mater. Chem. A*, 2018, **6**, 3850–3856.